Nano Research

Open Access

Research Article

Photothermoelectric effect-driven $TaSe_3$ tactile sensors for micrometer-scale distance detection

Gang Li[1], Xiaofei Ma[1], Lin Wu[1], Yanwei Sui[2] ✉, Jianglun Huang[3], Keke Huang[3] ✉, and Liang Li[1] ✉

[1] Anhui Key Laboratory of Nanomaterials and Nanotechnology, Institute of Solid State Physics, Hefei Institutes of Physical Science, Chinese Academy of Sciences, Hefei 230031, China
[2] Jiangsu Province Engineering Laboratory of High-Efficient Energy Storage Technology and Equipment, School of Materials Science and Physics, China University of Mining and Technology, Xuzhou 221116, China
[3] Ningbo Canmag Technology Co., Ltd, Ningbo 315105, China

Cite this article: *Nano Research*, **2026**, *19*, 94908913. https://doi.org/10.26599/NR.2026.94908913

ABSTRACT: Detecting human-robot distances at the micrometer-scale is essential for advanced human–robot interaction, yet existing flexible sensors are typically limited to millimeter-scale resolution. Here, we develop a flexible sensor using quasi-one-dimensional (quasi-1D) $TaSe_3$ nanowires to measure micrometer-scale distances via the photothermoelectric (PTE) effect. The sensor has self-powered operation (zero bias), ultrabroadband photoresponse (405 nm to 10.6 μm), good bending stability (no degradation after 500 bends), and strain-insensitive photocurrent. Importantly, it achieves 1 μm spatial resolution for distance detection within 100 μm, suggesting micrometer-scale sensitivity. These results highlight the potential of $TaSe_3$-based PTE sensors for advancing human-robot systems.

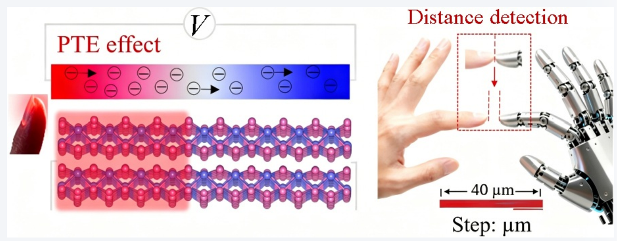

KEYWORDS: photothermoelectric (PTE) effect, $TaSe_3$, micrometer-scale distance detection, flexible tactile sensor

1 Introduction

Transition metal trichalcogenides TMTs (M = Ti, Zr, Hf, Ta, and Nb; X = S, Se, and Te) is a type of unique quasi-one-dimensional (1D) layered materials, which have led to significant advancements in the field of physics and hold great potential for practical applications across various technological domains [1–4]. Especially, topological semimetal candidate $TaSe_3$ materials are highly appealing in emerging electronic technologies, such as topological surface states, superconductivity, high breakdown current density and excellent electromagnetic interference shielding [5–8]. As a quasi-1D layered transition metal trichalcogenide, $TaSe_3$ features a unique structure: strong in-plane covalent Ta-Se bonds and adjacent layers stacked in a planar manner via weak van der Waals interaction [9–12]. Such advantages suggest the superior flexibility of $TaSe_3$, a feature crucial for applications in flexible electronic sensors [13–16]. Moreover, $TaSe_3$ has recently demonstrated a prominent Seebeck coefficient, directly validating its potential as a photothermoelectric (PTE) sensor [17–19]. Since the PTE response depends on the temperature gradient, variations in thermal coupling induced by distance can be transduced into electrical signals.

Notably, distance-related tactile perception is crucial for enabling human-robot interaction, as it supports precise sensor-motor control for safe, accurate human interaction [20–22]. Despite significant advancements, a key challenge persists: the distance detection precision remains at the millimeter scale (> 1 mm) level [23–28]. The tactile sensors for human-robot interaction, particularly those capable of fine-distance detection, remain in their infancy. To address this challenge, it is anticipated that $TaSe_3$ is highly desirable for self-powered and tactile sensor.

In this work, we designed a flexible $TaSe_3$ nanowire-based sensor that leverages the PTE effect for micrometer-scale distance detection. To this end, we prepared high-quality quasi-1D $TaSe_3$ via chemical vapor transport (CVT)—the synthesized material features a silvery-white appearance and reaches several centimeters in length—and subsequently fabricated $TaSe_3$ devices. Using room-temperature scanning photocurrent microscopy (SPCM), we confirmed its PTE effect, and systematically characterized its photoresponse across a broadband range (405 nm to 10.6 μm)—verifying its ability to detect infrared radiation from human fingers. Critically, as a flexible sensor, it exhibits remarkable durability: no significant performance degradation after 500 bends, stable photoresponse over bending angles of $\theta = 0°$ to 80°, and a spatial

Received: March 30, 2026; **Revised:** May 22, 2026
Accepted: June 4, 2026

✉Address correspondence to Yanwei Sui, wyds123456@outlook.com; Keke Huang, hkk@canmag.cn; Liang Li, liliang@issp.ac.cn

resolution of 1 μm for distance detection within ~ 100 μm range.

2 Materials and methods

2.1 $TaSe_3$ growth and characterization

$TaSe_3$ was grown by a CVT method [29]. Raman spectra were conducted by a Raman system (FST2 Ahdx DZ, Zolix) [30]. X-ray photoelectron spectroscopy (XPS) was performed (ESCALAB 250Xi). The transmission electron microscope (TEM, Talos F200X, FEI) was used to examine the energy-dispersive X-ray spectroscopy (EDS) [31].

2.2 Device measurement

The electrical properties were performed in a probe station (HFS600E-PB4) using a semiconductor device parameter analyzer (Keithley 4200A-SCS). To test SPCM mapping, the 532 nm light spot was focused on the device with a 50× objective (NA = 0.42), and the laser spot was nearly flat with a size of about 2.5 μm. A 532 nm laser with tunable power was used to test the photoresponse of the devices. The 405, 635, 780, 940, 1035, and 1550 nm LED light sources were used to test the broadband wavelength response. A homemade wavelength-tunable multichannel mid-wave infrared (MWIR) laser (3.075 μm) was used to investigate the performance of the detector in the MWIR range. The diameter of the MWIR laser beam was ≈ 3 mm. The performance of the LWIR 10.6 μm was investigated using a CO_2 laser source. The optical power meter was used to calibrate laser power.

3 Results and discussion

The quasi-1D structure of $TaSe_3$ along the crystallographic b and c axes is depicted in Figs. 1(a) and 1(b), respectively [32]. $TaSe_3$ crystallizes into a monoclinic layered structure characterized with the space group $P2_1/m$ (No. 11) [33]. The fundamental building blocks consist of two types of parallel trigonal-prismatic chains aligned along the b axis, which together form the quasi-1D crystal structure by weak van der Waals (vdW) force [33]. Each chain is formed by a linear arrangement of irregular prismatic cages, with six selenium (Se) atoms located at the corners and a single tantalum (Ta) atom located at the center [33]. Weak vdW bonding between chains allows $TaSe_3$ cleavage into nanowires [29]. $TaSe_3$ crystals were prepared via CVT method (Fig. S1 in the Electronic Supplementary Material (ESM)), with growth details in the Experimental section [32]. Figure 1(c) shows SEM images of nanowires obtained via mechanical exfoliation. The nanowires display a curved morphology without any damage, suggesting that $TaSe_3$ has promising potential as a flexible sensor for practical applications. Figure 1(d) presents the elemental composition of $TaSe_3$ by XPS. Peaks at ~ 23, 37, and 45 eV binding energy correspond to Ta $4f_{7/2}$, $5p_{3/2}$, and $5p_{1/2}$, respectively, while the signals at ~ 54 eV is attributed to Se $3d_{5/2}$ [5]. EDS further confirmed the composition of $TaSe_3$. Figures 1(h) and 1(i) show prominent Ta and Se signals, confirming its composition and homogeneous element distribution. Additionally, Raman analysis under parallel and perpendicular polarized configurations showed notable peaks at 238, 214, 185, 176, 164, 140, 126, and 108 cm^{-1} (Fig. 1(e)). These peaks correspond to A_{1g}, A_{1g}, B_2/A_g, B_2/A_g, A_{1g}, A_{1g}, B_g, and A_g vibrational modes [34]. To investigate the anisotropy of phonon vibrations, angle-resolved polarized Raman (ARPR) spectroscopy was conducted using the $TaSe_3$ nanowire. Raman intensity shows distinct periodic variations under parallel polarization (Fig. 1(f)). Polarization angle was systematically varied from 0° to 360° in 15° increments (Fig. S2 in the ESM). The polarized scattering signals were collected in a parallel configuration relative to the incident light polarization. These data shows clear angular dependence of Raman intensity on light illumination, indicating pronounced in-plane anisotropic phonon vibrations. Interlayer vibration and thermal expansion of $TaSe_3$ were studied via temperature-dependent Raman spectroscopy (80–300 K, Fig. S3 in the ESM). Results show a pronounced Raman peak red shift with increasing temperature (Fig. S3(a) in the ESM). Extracted interlayer interaction information is shown in Fig. S3(b) in the ESM. The solid curves in Fig. S3(b) in the ESM were linearly fitted using: $\omega(T) = \omega_0 + \chi T$, where χ, ω_0 and T denote the first-order temperature coefficient, phonon frequency and temperature, respectively [17]. The absolute values of χ for the Raman modes were determined to be 0.01094, 0.01591, 0.00653, 0.01286, 0.01789, 0.01286, and 0.00807 $cm^{-1}\cdot K^{-1}$. The χ parameter describes the slope of the fitted line and is positively correlated with the degree to which temperature influences the interlayer vibration between adjacent layers.

To explore electronics and photoelectronics applications, we fabricated sensors using mechanically exfoliated $TaSe_3$ nanowires and systematically characterized their properties. Resistance shows a positive correlation with temperature, indicating typical metallic behavior (Fig. S4 in the ESM). Additionally, we examined thermoelectric performance by measuring the Seebeck coefficient (S)—which quantifies the ability to convert temperature difference (ΔT) to electrical voltage (ΔU), defined by the equation $S = -\Delta U/\Delta T$. The measured Seebeck coefficient was found to be −12.6 $\mu V\cdot K^{-1}$ (Fig. 2(b)) [35, 36]. Next, the photoresponse of the sensor was measured at room temperature. The sensor exhibits photocurrent at zero bias when light is focused on one end of the sensor (Fig. 2(c)). Additionally, temporal response under 532 nm light (0 V bias) indicates self-powered operation (Fig. 2(d). In addition, a response time of 11.7 ms can be achieved in our sensor as shown in Fig. S5 in the ESM. The estimated −3 dB bandwidth is approximately 30 Hz according to $f_c = 1/(2\pi\tau)$. To investigate the photodetection mechanism of $TaSe_3$ sensors, SPCM images without extra voltage are presented in Fig. 2(e). Photocurrent signals are obtained from the $TaSe_3$-metal interface and surrounding areas, with nonlocal photoresponse observed via light illumination. Notably, the $TaSe_3$ sensor demonstrates stable operation at zero bias, indicating its self-powered characteristics. Common photodetection mechanisms include three primary types: photovoltaic (PV) effect, photo-Dember (PD) effect, and PTE effect [37]. The PV effect, which stems from the built-in electric field, is associated with a Schottky contact, leading to a nonlinear I–V curve and a photocurrent distribution at the $TaSe_3$-electrode interface. In our sensor, ohmic contacts and the photoresponse away from electrodes rule out the PV effect. The photoresponse associated with the PD effect occurs in the contact region of $TaSe_3$ and electrode, where electron-hole symmetry is broken. Consequently, the photocurrent in $TaSe_3$ sensor is not restricted to the contact regions, further ruling out the PD effect. Overall, neither the PV nor PD effect explains the characteristics of $TaSe_3$ sensor. In contrast, the PTE effect produces both ohmic contacts and nonlocal photocurrent, consistent with our results. Unlike mechanisms such as photogating or PD, the PTE effect enables ultrabroadband photodetection without bias at room temperature [38]. The

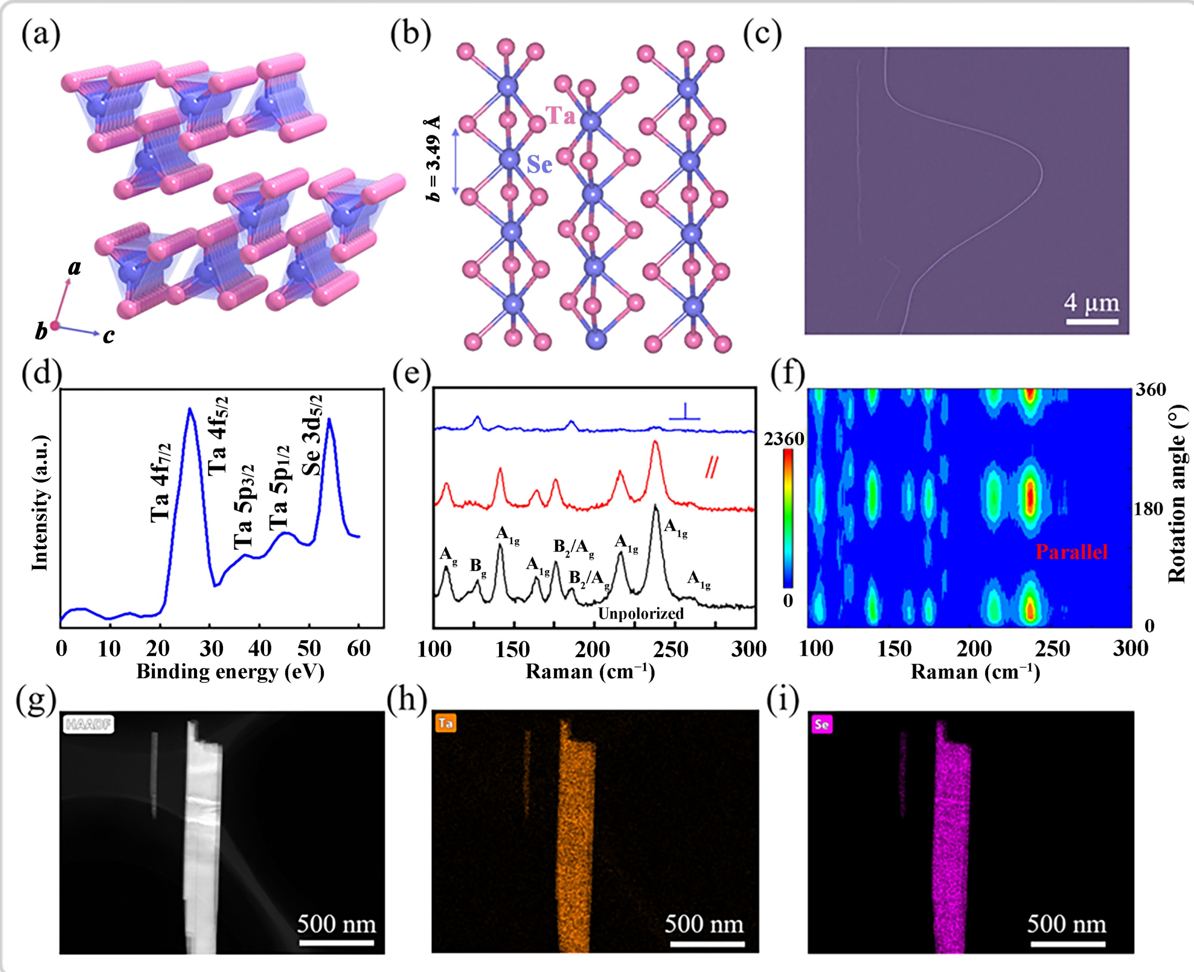

Figure 1 Illustration of the quasi-1D structural characterizations of $TaSe_3$ nanowire. (a) and (b) Structural model of 1D crystals from different directions. (c) SEM image of exfoliated $TaSe_3$ nanowires. (d) XPS spectrum of Ta and Se. (e) Raman spectra of $TaSe_3$ sample under parallel and perpendicular polarized configurations. (f) False-color plots of polarized Raman intensities under parallel polarization configurations. Corresponding EDS elemental mapping images for (h) Ta and (i) Se. The scale bar is 500 nm.

photocurrent is linearly proportional to the optical power (Fig. 2(f)). Figure S6 in the EMS shows the magnitude of the temperature gradient generated under illumination conditions. For instance, infrared radiation emitted by a human finger approaching the end of a PTE sensor can induce a measurable potential difference, which shows a linear correlation with the finger-sensor distance (Fig. 2(g)). Figure S7 in the ESM shows the infrared response detection capability. The distance-dependent response originates from modulated photothermal radiation rather than direct geometric distance measurement. Building on this validated distance-sensing capability, Fig. 2(h) schematically shows human-robot interaction: The robotic hand adjusts movements using PTE sensor distance data. This highlights how accurate sensing enables responsive interaction, with red dashed lines marking guiding distance variations. Thus, micrometer-scale detection is feasible with the $TaSe_3$-based PTE sensor. For experimental validation of this feedback mechanism, Fig. 2(i) shows the time-resolved photocurrent of the PTE sensor during human finger approach/withdrawal. The PTE mechanism achieves micrometer scale-resolution. The high resolution shows great potential in distance-related tactile sensors (Table S1 in the ESM). P_0 is defined as the photocurrent detected by the sensor at a 100 µm sensing distance for different target objects, while the photocurrent variation caused exclusively by distance change is defined as ΔP (Fig. 2(i)). ΔP is given by $\Delta P = (S{\cdot}\Delta T)/R$, with ΔT the temperature difference, S the Seebeck coefficient, and R the resistance. Thus, different targets can be detected by $TaSe_3$ sensor.

Ambient temperature and bending angle constitute critical factors affecting sensor performance in practical implementations. Experimental results demonstrate relatively stable performance across a broad temperature range (80–280 K), with ohmic contact integrity maintained even under temperature cycling conditions (Fig. 3(a)). To validate its suitability applications, the temperature coefficient of resistance (TCR) of the $TaSe_3$ nanowires is 0.00174 K^{-1}, showing the potential in a broad temperature range (Fig. S8 in the ESM). Flexible nanowires exhibit enhanced adaptability to irregular or curved surfaces, making them suitable for applications requiring integration with complex geometries [4, 14]. As previously mentioned, $TaSe_3$ nanowires have inherent flexibility, making it suitable for fabricating a flexible sensor by integrating $TaSe_3$ with a polyethylene terephthalate (PET) substrate [39]. To validate its suitability for applications (where repeated bending is inevitable), we characterized the bending stability. Figure 3(b) presents the photocurrent of the flexible sensor over 500 bending cycles [13, 16]. Notably, the photocurrent characteristics remained well-preserved even after extensive bending, confirming the exceptional bending

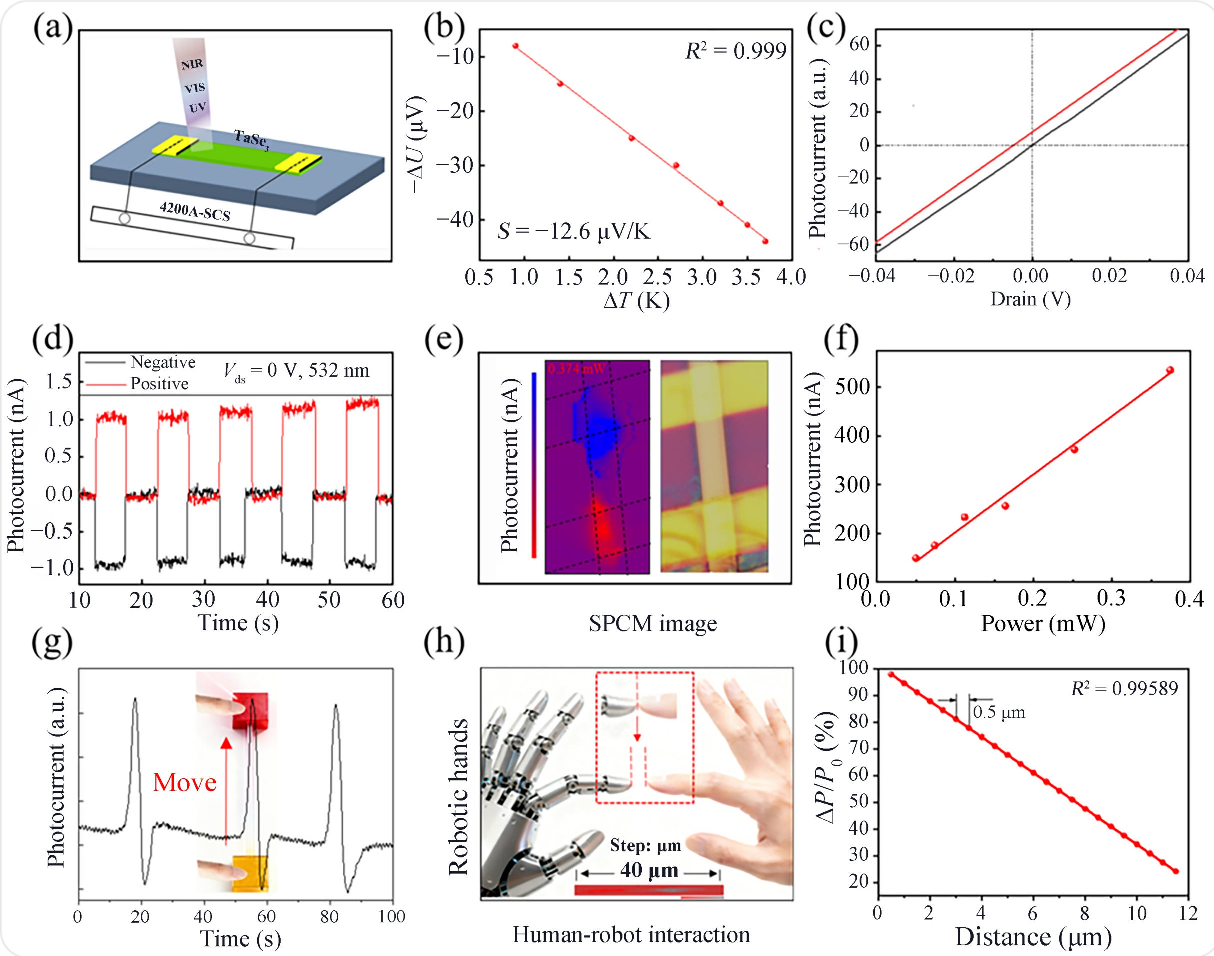

Figure 2 Photothermoelectric effect and distance detection of the $TaSe_3$ sensor. (a) Schematic of $TaSe_3$-based sensor. (b) Voltage across the $TaSe_3$ versus the corresponding temperature difference to determine the room-temperature Seebeck coefficient of $TaSe_3$. The red line is the linear fit to the experimental data, and the resulting coefficient of determination (R^2) is 0.999. (c) Output characteristics in the dark (black solid line) and under illumination (red solid line) of $TaSe_3$ sensor. (d) Temporal response with the light spot positioned on the top $TaSe_3$/Au interface (top-interface) and bottom one (bottom-interface). (e) SPCM images of the $TaSe_3$ sensor at zero bias with 532 nm excitation. (f) The photocurrent intensity as a function of light power. The solid lines represent the linear fit. (g) Distance detection using a $TaSe_3$ sensor during human finger approach and withdrawal. (h) In the distance detection, red dashed lines mark distance variations—guiding interaction and enabling precise coordination. (i) The PTE mechanism achieves micrometer scale resolution. The moving distance intervals between the sensor and the detection target is 0.5 μm. P_0 is defined as the photocurrent detected by the sensor at a 100 μm sensing distance for different target objects, while the photocurrent variation caused exclusively by distance change is defined as ΔP.

endurance and mechanical flexibility. Figures 3(c) and 3(d) illustrates the normalized photocurrent of the self-powered sensor during prolonged operation at four distinct bending angles: 100°, 125°, 145°, and 180° (non-bent) under light illumination [15]. The sensor performs stably across these angles, with no significant photocurrent variation. The $TaSe_3$ sensor shows strain-insensitive photocurrent. Given this adaptability, we investigated the photoresponse of a $TaSe_3$ nanowire-based sensor across a broad wavelength range (405–3075 nm) under zero-bias operation (Fig. S9 in the ESM) [40]. Figure S9(c) in the ESM shows ultrabroadband detection up to 10.6 μm. Figure S10 in the ESM revealed a linear relationship between photocurrent intensity and incident light power.

For practical application, we integrated the $TaSe_3$ sensor into a robotic hand (Fig. 4(a)). Figure 4(a) also illustrates the fingertip-integrated $TaSe_3$ PTE sensor working principle in human-robot interaction, with three stages: (I) sensing (fingertip PTE sensor captures stimuli), (II) data processing (brain-like signal analysis), and (III) motor actuation (drives adaptive robotic motions) [41]. The PTE sensor—serving as the core fingertip component—enables precise interactive feedback. For experimental validation of this feedback mechanism, Fig. 4(b) shows the time-resolved photocurrent of the PTE sensor during approach/withdrawal. The rise time is 50 ms and the fall time is 60 ms. To verify the detection capability at the micrometer-scale, a light spot (simulating a heat source) was moved toward the sensor at 1 μm·s^{-1}; Fig. 4(b) shows photocurrent variation distinguishes micrometer-scale movements. To repeatedly verify the high-resolution distance detection within ~ 100 μm, we brought infrared light near the sensor with 30 μm distance intervals. Figure S11 in the ESM shows that $TaSe_3$ sensor photocurrent variation clearly distinguishes movements. The photoresponse shows no change under ambient light (Fig. S12 in the ESM).

4 Conclusion

In this study, we developed a PTE-based tactile sensor to address a key challenge in robotics: the lack of mature fine-distance detection

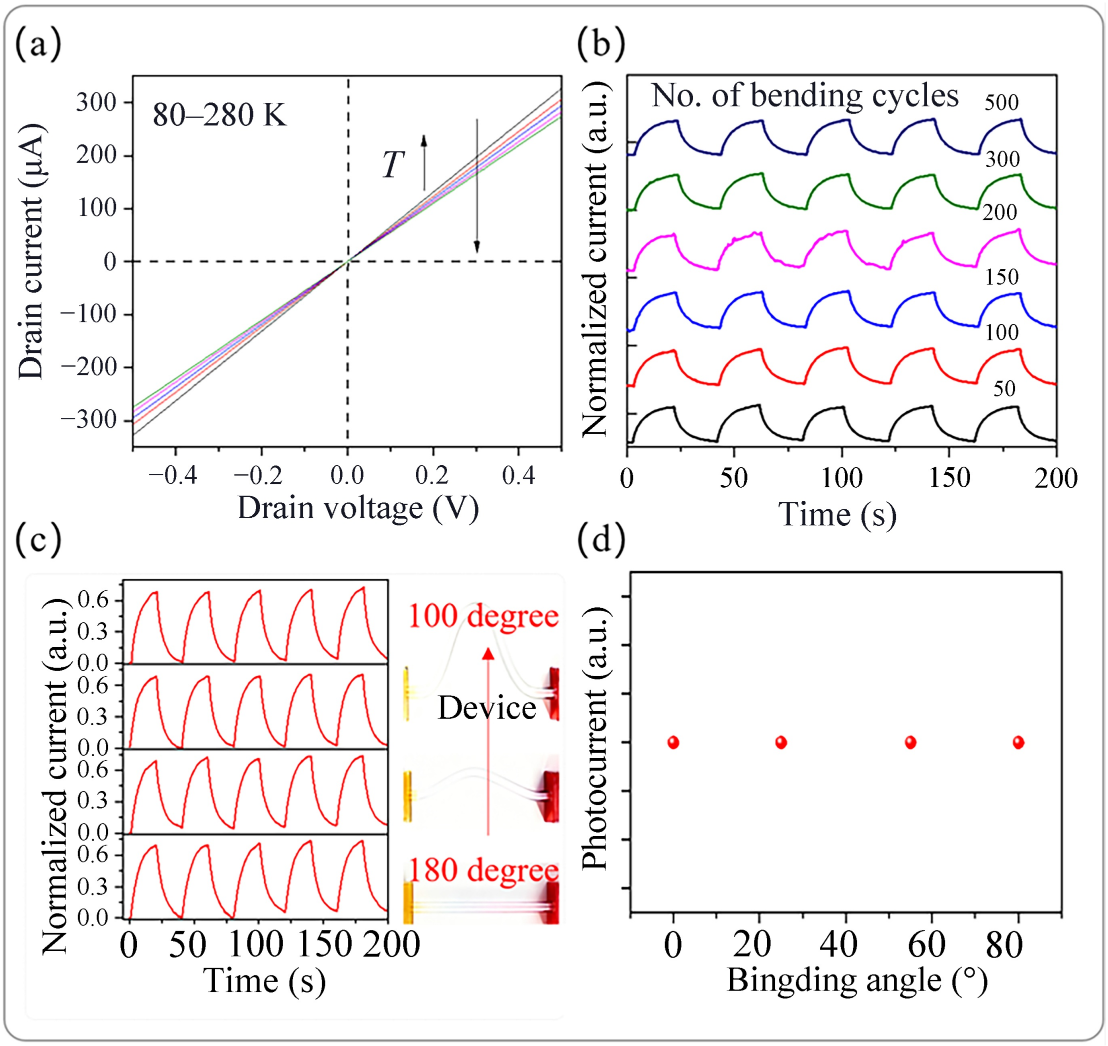

Figure 3 The stability and flexibility of the $TaSe_3$ sensor. (a) Temperature-dependent output curves of the $TaSe_3$ sensor. (b) The photoresponse curves of the sensor after different numbers of repetitive bending cycles. (c) and (d) The self-powered sensor features stable performance upon repeated bending at various angles of curvature (100°, 125°, 145°, and 180°), which shows strain-insensitive photocurrent.

sensors. The PTE effect is the key working mechanism: asymmetric light induces sensor temperature differences, generating an electric potential difference with a linear correlation to human finger-sensor distance. For this design, we selected a flexible quasi-1D topological semimetal material with a confirmed Seebeck coefficient as the key sensing material for its suitability in PTE-based distance detection. The sensor precisely detects micrometer-scale distances, enabling adaptive interaction. This work demonstrates the feasibility of PTE-based distance-dependent response and its vital role in advancing dexterous robotic systems.

Electronic Supplementary Material: Supplementary material (Fig. S1 Schematic of CVT method; Fig. S2 Angle dependence of the Raman intensities under parallel polarization configurations; Fig. S3 Temperature-dependent Raman spectroscopy of $TaSe_3$; Fig. S4 Temperature-dependent resistance from 80 to 280 K; Fig. S5 The temporal response time under 532 nm; Fig. S6 The magnitude of the temperature gradient generated under different light power (532 nm laser); Fig. S7 The positive (red) and negative (black) photocurrent response under 1064 nm; Fig. S8 The temperature coefficient of resistance (TCR) of $TaSe_3$ nanowires under 80–280 K; Fig. S9 Photoresponse of the self-powered $TaSe_3$ sensor under different light illumination (405 to 1035 nm); Fig. S10 Photoresponse of the $TaSe_3$ sensor for different excitation wavelengths at room temperature; Fig. S11 The resolution of distance-detection sensor with 30 μm intervals; Fig. S12 The photoresponse under dark and ambient light; and Table S1 Comparison of distance detection performance in the literature) is available in the online version of this article at https://doi.org/10.26599/NR.2026.94908913.

Data availability

All data needed to support the conclusions in the paper are presented in the manuscript and the Electronic Supplementary Material. Additional data related to this paper may be requested from the corresponding author upon request.

Acknowledgements

This work is supported by the National Natural Science Foundation of China (No. 52572187), the China Postdoctoral Science Foundation (No. 2023M733544), and the Postdoctoral Fellowship

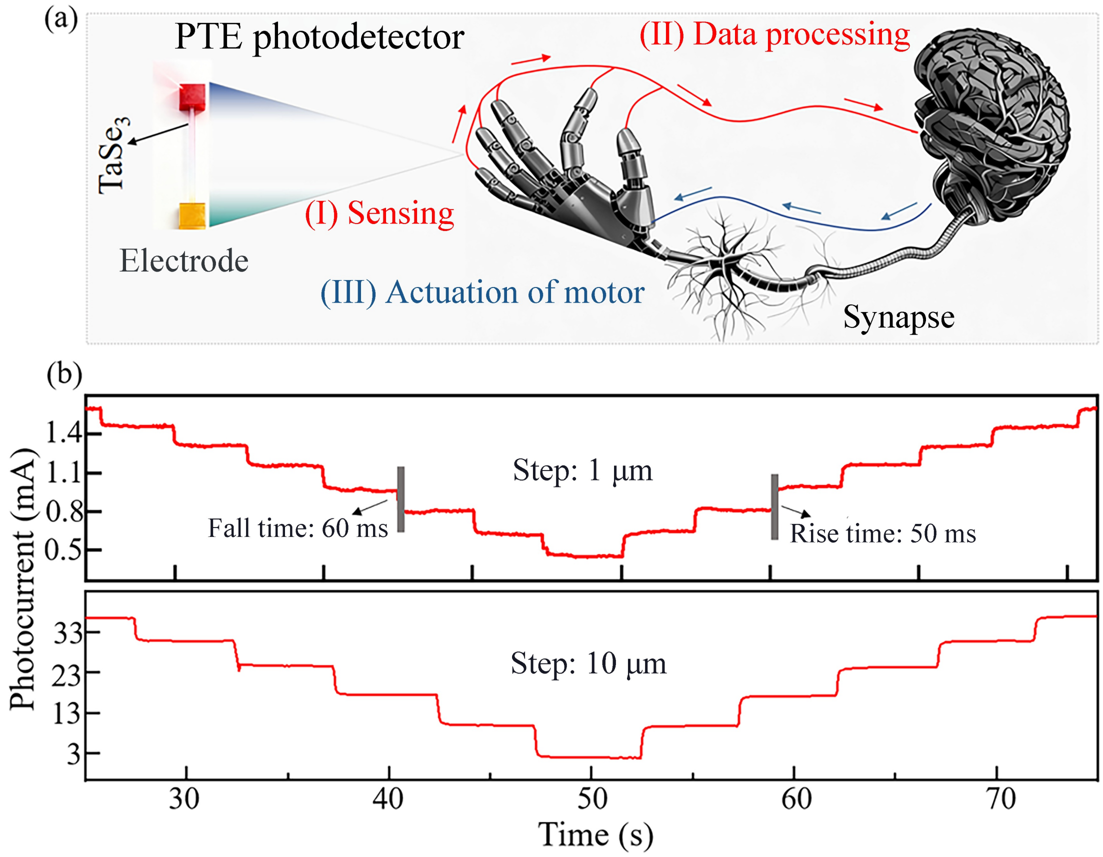

Figure 4 The capability of micrometer-scale distance detection. (a) Schematic of the overall structure of the finger-shaped tactile sensor inspired by human fingers. (b) The moving distance intervals between the sensor and the detection target are 1 and 10 μm, respectively. The rise/fall time: 50/60 ms.

Program of CPSF (No. GZC20232721).

Declaration of competing interest

The authors declare no conflict of interests in this work

Author contribution statement

G. L. and L. L. conceived the idea and performed the experimentsand investigated and wrote the whole manuscript. X. F. M., L. W., Y. W. S., J. L. H., and K. K. H. participated in data analysis and manuscript discussion. All authors participated in data analysis and manuscript discussion.

Use of AI statement

None.

References

[1] Chen, X.; Chen, B. K.; Jiang, B.; Gao, T. F.; Shang, G.; Han, S. T.; Kuo, C. C.; Roy, V. A. L.; Zhou, Y. Nanowires for UV-vis-IR optoelectronic synaptic devices. *Adv. Funct. Mater.* **2023**, *33*, 2208807.

[2] Jeong, B. J.; Choi, K. H.; Jeon, J.; Yoon, S. O.; Chung, Y. K.; Sung, D.; Chae, S.; Kim, B. J.; Oh, S.; Lee, S. H. et al. Ternary transition metal chalcogenide $Nb_2Pd_3Se_8$: A new candidate of 1D Van der Waals materials for field-effect transistors. *Adv. Funct. Mater.* **2022**, *32*, 2108104.

[3] Meng, Y.; Wang, W.; Ho, J. C. One-dimensional atomic chains for ultimate-scaled electronics. *ACS Nano* **2022**, *16*, 13314–13322.

[4] Barani, Z.; Kargar, F.; Ghafouri, Y.; Ghosh, S.; Godziszewski, K.; Baraghani, S.; Yashchyshyn, Y.; Cywiński, G.; Rumyantsev, S.; Salguero, T. T. et al. Electrically insulating flexible films with quasi-1D van der Waals fillers as efficient electromagnetic shields in the GHz and Sub-THz frequency bands. *Adv. Mater.* **2021**, *33*, 2007286.

[5] Chen, C.; Liang, A. J.; Liu, S.; Nie, S. M.; Huang, J. W.; Wang, M. X.; Li, Y. W.; Pei, D.; Yang, H. F.; Zheng, H. J. et al. Observation of topological electronic structure in quasi-1D superconductor $TaSe_3$. *Matter* **2020**, *3*, 2055–2065.

[6] Lin, C.; Ochi, M.; Noguchi, R.; Kuroda, K.; Sakoda, M.; Nomura, A.; Tsubota, M.; Zhang, P.; Bareille, C.; Kurokawa, K. et al. Visualization of the strain-induced topological phase transition in a quasi-one-dimensional superconductor $TaSe_3$. *Nat. Mater.* **2021**, *20*, 1093–1099.

[7] Ma, J. Z.; Nie, S. M.; Gui, X.; Naamneh, M.; Jandke, J.; Xi, C. Y.; Zhang, J. L.; Shang, T.; Xiong, Y. M.; Kapon, I. et al. Multiple mobile excitons manifested as sidebands in quasi-one-dimensional metallic $TaSe_3$. *Nat. Mater.* **2022**, *21*, 423–429.

[8] Nomura, A.; Yamaya, K.; Takayanagi, S.; Ichimura, K.; Tanda, S. Effect of Cu doping on superconductivity in $TaSe_3$: Relationship between superconductivity and induced charge density wave. *Europhys. Lett.* **2019**, *124*, 67001.

[9] Debnath, T.; Debnath, B.; Lake, R. K. Thermal conductivity of the quasi-one-dimensional materials $TaSe_3$ and $ZrTe_3$. *Phys. Rev. Mater.* **2021**, *5*, 034010.

[10] Gatti, G.; Gosálbez-Martínez, D.; Wu, Q. S.; Hu, J.; Zhang, S. N.; Autès, G.; Puppin, M.; Bugini, D.; Berger, H.; Moreschini, L. et al. Origin of large magnetoresistance in the topological nonsymmorphic semimetal $TaSe_3$. *Phys. Rev. B* **2021**, *104*, 155122.

[11] Hyun, J.; Jeong, M. Y.; Jung, M. C.; Lee, Y.; Kim, Y.; Jung, S.; Seok, B.; Song, J.; Lim, C. Y.; Cha, J. et al. Strain-controlled evolution of

electronic structure indicating topological phase transition in the quasi-one-dimensional superconductor $TaSe_3$. *Phys. Rev. B* **2022**, *105*, 115143.

[12] Yang, X. C.; Luo, X.; Gao, J. J.; Jiang, Z. Z.; Wang, W.; Wang, T. Y.; Si, J. G.; Xi, C. Y.; Song, W. H.; Sun, Y. P. Planar Hall effect in the quasi-one-dimensional topological superconductor $TaSe_3$. *Phys. Rev. B* **2021**, *104*, 155106.

[13] Wu, W. Q.; Wang, X. D.; Han, X.; Yang, Z.; Gao, G. Y.; Zhang, Y. F.; Hu, J. F.; Tan, Y. W.; Pan, A. L.; Pan, C. F. Flexible photodetector arrays based on patterned $CH_3NH_3PbI_{3-x}Cl_x$ perovskite film for real-time photosensing and imaging. *Adv. Mater.* **2019**, *31*, 1805913.

[14] Sun, H. X.; Tian, W.; Cao, F. R.; Xiong, J.; Li, L. Ultrahigh-performance self-powered flexible double-twisted fibrous broadband perovskite photodetector. *Adv. Mater.* **2018**, *30*, 1706986.

[15] Leung, S. F.; Ho, K. T.; Kung, P. K.; Hsiao, V. K. S.; Alshareef, H. N.; Wang, Z. L.; He, J. H. A self-powered and flexible organometallic halide perovskite photodetector with very high detectivity. *Adv. Mater.* **2018**, *30*, 1704611.

[16] Hu, W.; Huang, W.; Yang, S. Z.; Wang, X.; Jiang, Z. Y.; Zhu, X. L.; Zhou, H.; Liu, H. J.; Zhang, Q. L.; Zhuang, X. J. et al. High-performance flexible photodetectors based on high-quality perovskite thin films by a vapor-solution method. *Adv. Mater.* **2017**, *29*, 1703256.

[17] Li, G.; Yin, S. Q.; Tan, C. Y.; Chen, L. J.; Yu, M. X.; Li, L.; Yan, F. Fast photothermoelectric response in CVD-grown $PdSe_2$ photodetectors with in-plane anisotropy. *Adv. Funct. Mater.* **2021**, *31*, 2104787.

[18] Li, G.; Zhang, H. L.; Li, Y.; Yin, S. Q.; Kan, X. C.; Wei, W. S.; Du, H. F.; Ge, B. H.; An, C.; Tian, M. L. et al. Ultra-broadband, fast, and polarization-sensitive photoresponse of low-symmetry 2D $NdSb_2$. *Nano Res.* **2022**, *15*, 5469–5475.

[19] Fisher, B. Thermoelectric power and elastoresistance of $TaSe_3$. *Phys. Rev. B* **1987**, *35*, 2687–2689.

[20] Lin, Y. Y.; Raj, R.; Juang, J. Y. A comprehensive review of dexterous robotic hands: Design, implementation, and evaluation. *Bioinspir. Biomim.* **2025**, *20*, 041003.

[21] Zhang, Y. T.; Gao, P.; Wang, Z. Y.; He, Q. L. Research on status monitoring and positioning compensation system for digital twin of parallel robots. *Sci. Rep.* **2025**, *15*, 7432.

[22] He, J. Q.; Wei, R. L.; Ma, X. L.; Wu, W. Q.; Pan, X. J.; Sun, J. L.; Tang, J. Q.; Xu, Z. S.; Wang, C. F.; Pan, C. F. Contactless user-interactive sensing display for human-human and human-machine interactions. *Adv. Mater.* **2024**, *36*, 2401931.

[23] Zhang, J. H.; Yao, H. M.; Mo, J. Y.; Chen, S. Y.; Xie, Y.; Ma, S. L.; Chen, R.; Luo, T.; Ling, W. S.; Qin, L. F. et al. Finger-inspired rigid-soft hybrid tactile sensor with superior sensitivity at high frequency. *Nat. Commun.* **2022**, *13*, 5076.

[24] Pyo, S.; Lee, J.; Bae, K.; Sim, S.; Kim, J. Recent progress in flexible tactile sensors for human-interactive systems: From sensors to advanced applications. *Adv. Mater.* **2021**, *33*, 2005902.

[25] Liu, W. B.; Duo, Y. N.; Liu, J. Q.; Yuan, F. Y.; Li, L.; Li, L. C.; Wang, G.; Chen, B. H.; Wang, S. Q.; Yang, H. et al. Touchless interactive teaching of soft robots through flexible bimodal sensory interfaces. *Nat. Commun.* **2022**, *13*, 5030.

[26] Qi, M.; Xu, R. Z.; Ding, G. L.; Zhou, K.; Zhu, S. R.; Leng, Y. B.; Sun, T.; Zhou, Y.; Han, S. T. An in-sensor humidity computing system for contactless human-computer interaction. *Mater. Horiz.* **2024**, *11*, 939–948.

[27] Jiang, C. P.; Xu, H. H.; Yang, L.; Liu, J. Q.; Li, Y.; Takei, K.; Xu, W. T. Neuromorphic antennal sensory system. *Nat. Commun.* **2024**, *15*, 2109.

[28] Kamijo, T.; van Breemen, A. J. J. M.; Ma, X.; Shanmugam, S.; Bel, T.; de Haas, G.; Peeters, B.; Petre, R.; Tordera, D.; Verbeek, R. et al. A touchless user interface based on a near-infrared-sensitive transparent optical imager. *Nat. Electron.* **2023**, *6*, 451–461.

[29] Liu, G. X.; Rumyantsev, S.; Bloodgood, M. A.; Salguero, T. T.; Shur, M.; Balandin, A. A. Low-frequency electronic noise in quasi-1D $TaSe_3$ van der Waals nanowires. *Nano Lett.* **2017**, *17*, 377–383.

[30] Zeng, C.; Xu, Y. S.; Wei, X. Q.; Liang, J. N.; Sun, Z. D.; He, X. Y.; Du, G. F.; Wang, S. H.; Liu, Y.; Zhou, X. et al. A universal all-dry microfabrication method for sensitive electronic materials via an inorganic molecular lithographic mediator. *Nat. Commun.* **2026**, *17*, 2098.

[31] Qin, L. H.; Guan, P. F.; Shao, J. F.; Xiao, Y.; Yu, Y. M.; Su, J.; Zhang, C. H.; Li, Y. Y.; Liu, S. H.; Li, P. Y. et al. Molecular crystal memristors. *Nat. Nanotechnol.* **2025**, *20*, 1641–1647.

[32] Saleheen, A. I. U.; Chapai, R.; Xing, L. Y.; Nepal, R.; Gong, D. L.; Gui, X.; Xie, W. W.; Young, D. P.; Plummer, E. W.; Jin, R. Y. Evidence for topological semimetallicity in a chain-compound $TaSe_3$. *npj Quantum Mater.* **2020**, *5*, 53.

[33] Stolyarov, M. A.; Liu, G. X.; Bloodgood, M. A.; Aytan, E.; Jiang, C. L.; Samnakay, R.; Salguero, T. T.; Nika, D.; Rumyantsev, S.; Shur, M. et al. Breakdown current density in *h*-BN-capped quasi-1D $TaSe_3$ metallic nanowires: Prospects of interconnect applications. *Nanoscale* **2016**, *8*, 15774–15782.

[34] Yang, J.; Wang, Y. Q.; Zhang, R. R.; Ma, L.; Liu, W.; Qu, Z.; Zhang, L.; Zhang, S. L.; Tong, W.; Pi, L. et al. Observation of charge density wave transition in $TaSe_3$ mesowires. *Appl. Phys. Lett.* **2019**, *115*, 033102.

[35] Dai, M. J.; Wang, C. W.; Qiang, B.; Jin, Y. H.; Ye, M.; Wang, F. K.; Sun, F. Y.; Zhang, X. R.; Luo, Y.; Wang, Q. J. Long-wave infrared photothermoelectric detectors with ultrahigh polarization sensitivity. *Nat. Commun.* **2023**, *14*, 3421.

[36] Koepfli, S. M.; Baumann, M.; Gadola, R.; Nashashibi, S.; Koyaz, Y.; Rieben, D.; Güngör, A. C.; Doderer, M.; Keller, K.; Fedoryshyn, Y. et al. Controlling photothermoelectric directional photocurrents in graphene with over 400 GHz bandwidth. *Nat. Commun.* **2024**, *15*, 7351.

[37] Zhu, B. X.; Zhu, C. Y.; Qin, J. K.; He, W.; Yue, L. Q.; Huang, P. Y.; Li, D.; Sun, R. Y.; Ye, S.; Du, Y. et al. Two-dimensional SnP_2Se_6 with gate-tunable Seebeck coefficient for telecommunication band photothermoelectric detection. *InfoMat* **2024**, *6*, e12600.

[38] Huang, J. Y.; You, C. Y.; Wu, B. M.; Wang, Y. Q.; Zhang, Z. Y.; Zhang, X. Y.; Liu, C.; Huang, N. G.; Zheng, Z.; Wu, T. Q. et al. Enhanced photothermoelectric conversion in self-rolled tellurium photodetector with geometry-induced energy localization. *Light: Sci. Appl.* **2024**, *13*, 153.

[39] Nie, Q. Y.; Wang, F.; Yang, F. S.; Xun, H. Z.; Hou, J. C.; Xu, Q. Y.; Hong, Y.; Zhang, J. Y.; Wei, X. Y.; Lin, Y. F. et al. Intelligent tactile perception revolution: Innovations in flexible FET-based tactile sensors for next-gen human-machine interfaces. *Adv. Mater.* **2026**, *38*, e10646.

[40] Li, X.; Liu, K. X.; Wu, D.; Lin, P.; Shi, Z. F.; Li, X. J.; Zeng, L. H.; Chai, Y.; Lau, S. P.; Tsang, Y. H. Van der Waals hybrid integration of 2D semimetals for broadband photodetection. *Adv. Mater.* **2025**, *37*, 2415717.

[41] Gautham, V.; Panpalia, A.; Manouchehri, H.; Gabani, K. K.; Anil, V.; Yerneni, S.; Thakar, R.; Nayyar, A.; Payare, M. A.; Jorgensen, E. et al. Slip-actuated bionic tactile sensing system with dynamic DC generator integrated E-textile for dexterous robotic manipulation. *Nat. Commun.* **2025**, *16*, 7005.